

## Article

# Micro/Nano Indentation Testing of Spark Plasma Sintered $\text{Al}_2\text{O}_3 + \text{ZrO}_2 + \text{cBN}$ Ceramics

Richard Sedlák <sup>1,\*</sup>, Michal Ivor <sup>1,2</sup>, Piotr Klimczyk <sup>3</sup>, Piotr Wyzga <sup>3</sup>, Marcin Podsiadlo <sup>3</sup>, Marek Vojtko <sup>1</sup> and Ján Dusza <sup>1</sup>

<sup>1</sup> Institute of Materials Research, Slovak Academy of Sciences, Watsonova 47, 040 01 Košice, Slovakia; mivor@saske.sk (M.I.); mvojtko@saske.sk (M.V.); jdusza@saske.sk (J.D.)

<sup>2</sup> Faculty of Materials, Metallurgy and Recycling, Technical University of Košice, Letná 9, 040 01 Košice, Slovakia

<sup>3</sup> Łukasiewicz Research Network–Krakow Institute of Technology, Zakopianska 73, 30-418 Krakow, Poland; piotr.klimczyk@kit.lukasiewicz.gov.pl (P.K.); piotr.wyzga@kit.lukasiewicz.gov.pl (P.W.); marcin.podsiadlo@kit.lukasiewicz.gov.pl (M.P.)

\* Correspondence: rsedlak@saske.sk; Tel.: +421-55-792-2400; Fax: +421-55-792-2408

**Abstract:**  $\text{Al}_2\text{O}_3 + 30 \text{ vol}\% \text{ZrO}_2$  matrix composites with 20 and 30 vol% cBN have been prepared with the optimized processing route, using spark plasma sintering (SPS) at temperatures of 1400 °C and 1250 °C. The influence of cBN addition on the microstructure characteristics, micro/nanohardness, elastic modulus, and crack-extension resistance of the composites and their constitutions have been investigated using scanning electron microscopy (SEM), statistical analyses of the individual grain size and micro/nanoindentation methods. The matrix consists of alumina and zirconia grains with grain sizes/diameter of approximately 220 and 160 nm with approximately 1.9  $\mu\text{m}$  cBN grains in the  $\text{Al}_2\text{O}_3 + \text{ZrO}_2 + \text{cBN}$  composites. The microhardness is slightly increasing with cBN addition from 16.2 to 17.1 GPa and the crack-extension resistance from 3.72 to 4.29  $\text{MPa}\cdot\text{m}^{1/2}$ . The toughening mechanisms are in the form of crack deflection, crack branching, and crack bridging. The nanohardness and indentation modulus of the matrix are approximately 30 and 420 GPa, and the cBN grains 70 and 777 GPa, respectively.

**Keywords:**  $\text{Al}_2\text{O}_3 + \text{ZrO}_2 + \text{cBN}$ ; micro/nano indentation; micro/nano hardness; crack-extension resistance



**Citation:** Sedlák, R.; Ivor, M.; Klimczyk, P.; Wyzga, P.; Podsiadlo, M.; Vojtko, M.; Dusza, J. Micro/Nano Indentation Testing of Spark Plasma Sintered  $\text{Al}_2\text{O}_3 + \text{ZrO}_2 + \text{cBN}$  Ceramics. *Ceramics* **2021**, *4*, 40–53. <https://doi.org/10.3390/ceramics4010004>

Received: 30 November 2020

Accepted: 11 January 2021

Published: 22 January 2021

**Publisher's Note:** MDPI stays neutral with regard to jurisdictional claims in published maps and institutional affiliations.



**Copyright:** © 2021 by the authors. Licensee MDPI, Basel, Switzerland. This article is an open access article distributed under the terms and conditions of the Creative Commons Attribution (CC BY) license (<https://creativecommons.org/licenses/by/4.0/>).

## 1. Introduction

Alumina ( $\text{Al}_2\text{O}_3$ ) ceramics, due to their excellent properties, such as high hardness, thermal stability, corrosion, and wear resistance, etc., are one of the most widely used advanced ceramics in different fields of industry, such as cutting tools, seal rings, components of bearings, etc. [1–4]. Despite the many attractive properties of  $\text{Al}_2\text{O}_3$  ceramics, the primary drawback limiting their wider application is their brittle nature, low fracture toughness. One of the well-known ways of improving fracture toughness is the development of zirconia toughened alumina (ZTA) composites [5–8]. In ZTA, the zirconia phase transformation is accompanied by a significant volume expansion, which generates compressive stresses resulting in reduced crack propagation, and improves fracture toughness of the system. Although the fracture toughness of ZTA ceramics is higher than that of  $\text{Al}_2\text{O}_3$  ceramics, it still does not meet all the requirements for materials in aerospace, machinery, automotive, and other fields of application. To further solve this problem, researchers in the past have used the addition of second-phase particles (titanium carbide, silicon carbide, titanium diboride, boron nitride, etc.) with higher physical and mechanical but also tribological properties to further improve the performance of alumina and ZTA ceramics [9,10].

Twenty years ago, Wang et al. [9] prepared  $\text{Al}_2\text{O}_3 + \text{ZrO}_2 + \text{SiC}$  composite powders by heterogeneous precipitation method and applied a hot press for densification of the

powders. The microstructure analyses of the system revealed that small  $ZrO_2$  particles were located within the  $Al_2O_3$  grains, while larger  $ZrO_2$  grains were located intergranularly between the  $Al_2O_3$  grains. According to the results, the SiC particles with nano-size located in the  $ZrO_2$  grains affected the phase transformation of  $ZrO_2$  and the mechanical properties of the ceramic. Recently, Chen et al. [10] reported results concerning the processing and characterization of  $Al_2O_3$ -mullite- $ZrO_2$ -SiC composites with high fracture toughness and bending strength. They reported that the processing at 1530 °C and the addition of 20% SiC results in high flexural strength and very high fracture toughness with values of 970 MPa and 12.3 MPa.m<sup>1/2</sup>, respectively. Several toughening mechanisms, such as crack deflection, phase transformation toughening, pull-out, and crack branching were found to contribute to the enhancement of the fracture toughness of the composite.

Cubic boron nitride (cBN) also has the potential for improving the mechanical and tribological properties of alumina and ZTA ceramics, owing to its excellent physical, mechanical, and chemical properties [11–15]. Due to its super hardness, good thermal conductivity, and good chemical resistance, not only as an additive, polycrystalline cBN has also been widely used in cutting tool applications. However, because of the strong covalent bonds, low self-diffusion coefficients of B and N, and the cBN to hBN phase transformation at high sintering temperatures, it is not easy to sinter cBN with high density using conventional sintering methods. The cBN to hBN phase transformation has been investigated by many researchers, and according to the results, when sintering at a high-temperature, cBN is only stable at high pressures [16,17]. These reports indicate that the fabrication of ceramic + BN composites with required properties under lower pressure is possible only at optimized processing conditions. Many researchers have prepared ceramic + BN composites using pressureless sintering (PS), hydrothermal hot pressing (HHP), hot isostatic pressing (HIP), and spark plasma sintering (SPS). The sintering behavior was found to be different for different composites. For example,  $Al_2O_3$  + 50 vol% cBN starts to shrink at 1200 °C, but  $Al_2O_3$  + 10 vol% cBN starts to shrink at lower temperatures of 1100 °C [11]. According to the investigations carried out during the last decade, spark plasma sintering (SPS), spark discharge via applied direct pulsed DC current generates internal localized heating promoting material transfer and local reactions as well as densification, can be a good technique for the processing of cBN-containing systems.

Hotta and Goto [15] sintered  $Al_2O_3$  + cBN composites containing 0 to 30 vol% cBN using SPS at temperatures between 1200 and 1600 °C under a pressure of 100 MPa. The highest fracture toughness and Vickers hardness (HV0.1) values were reported for the composite containing 20 vol% cBN sintered at 1300 °C with approximately 98% relative density, with values 4.1 MPa.m<sup>1/2</sup> and 26 GPa, respectively. The same authors [18] investigated the effects of cBN addition, phase transformation, and microstructure on the hardness of  $Al_2O_3$ -BN composites and constituents prepared from  $Al_2O_3$  and cBN powders using SPS. They reported that the hardness of the  $Al_2O_3$  matrix in the  $Al_2O_3$ -BN composites increased with decreasing sintering temperature and the hardness of the matrix for composites with cBN addition increased by 5 GPa compared to the value for monolithic  $Al_2O_3$  bodies prepared at the same temperature. According to the results, the hardness of cBN grains in the composite, processed at 1300 °C without the phase transformation of BN was 59 GPa at a load of 0.098 N, which decreased to 57 GPa for grains in composite sintered at 1400 °C due to a slight phase transformation from cBN to hBN.

Yaman and Mandal [19] recently investigated  $Al_2O_3$  composites containing MgO-stabilized  $ZrO_2$  sintered with 17.5 vol% of cBN addition by spark plasma sintering and demonstrate that cBN phase remained without transforming to hBN at the sintering temperature up to 1500 °C. The values of fracture toughness and hardness for alumina-based matrix were 4.64 MPa.m<sup>1/2</sup> and 18.75 HV10, respectively, while the fracture toughness and hardness of the  $Al_2O_3$  +  $ZrO_2$  + cBN composite were 5.26 MPa.m<sup>1/2</sup> and 16.74 GPa, respectively. The lower hardness of the composite was explained by the lower density.

Irshad et al. [20] prepared  $Al_2O_3$ -cBN/Ni composites using SPS processing route and studied the effect of  $Al_2O_3$  particle size and volume fraction of cBN additives, both with

and without nickel coating, on the microstructure characteristics, physical and thermo-mechanical properties of the composites. According to the results, cBN in a micro-sized alumina matrix transformed to hBN at a temperature of 1400 °C and a pressure of 50 MPa were applied, but no such transformation occurred for cBN grains in a nano-sized alumina matrix with nearly fully dense samples. The presence of nickel hindered the transformation of cBN into hBN and improved the interfacial bonding strength, which resulted in a more efficient load transfer and mechanical properties. Reducing the matrix particle size from micro- to nanosize was found to improve the hardness, with the 30 wt% cBN-Nano- $\text{Al}_2\text{O}_3$  composition showing the highest hardness value of 29 GPa and densification of 99%.

Very recently, Klimczyk et al. [21] investigated the sintering behavior, phase composition, microstructure characteristics, and mechanical properties of  $\text{Al}_2\text{O}_3$ -cBN based composites with an addition of TiN and  $\text{ZrO}_2$ , prepared by SPS. According to the results, Young's modulus of the systems sintered at different temperatures provides indirect, qualitative information on the cB→hBN transition, which seems to be even more sensitive than XRD analysis. The cubic phase of BN is not thermodynamically stable at ambient pressure and at temperatures higher than about 1300 °C [16,17]. Spark plasma sintering usually entails a pressure of up to 100 MPa, which is closer to ambient pressure than to the values of pressure in the cBN stability region, which are in the order of several GPa. During SPS, two opposing processes occur: Densification of the material (increase in density and Young's modulus), and cBN to hBN transformation at higher temperatures (decrease in density and Young's modulus). The phase composition of the composite has a greater impact on its Young's modulus than its density. They found that maxima on Young's modulus versus sintering temperature curves are more pronounced than on the corresponding densification curves.

The sintering behavior of the composites was found to be different in comparison to the sintering behavior of the  $\text{Al}_2\text{O}_3$  matrix. The Young's modulus of alumina increases with temperature up to 1250 °C and shows constant values for higher temperatures while the composites reach maximum values of Young's modulus at around the sintering temperature of 1300 °C. They reported that the addition of TiN promotes the formation of hBN most intensively, the  $\text{ZrO}_2$  moderately, and the pure  $\text{Al}_2\text{O}_3$  matrix the least. Significant improvement in fracture toughness was observed in all composites with a crack deflection at cBN grains as the main toughening mechanism. However, the addition of cBN does not result in the expected increase in the hardness of the composites.

The aim of the present contribution is the processing of  $\text{Al}_2\text{O}_3 + \text{ZrO}_2 + \text{cBN}$  composites with optimized processing route and an investigation of the influence of cBN addition on their microstructure development, microhardness, and crack-extension resistance. Further aims are to measure the nanohardness of the matrix and cBN grains.

## 2. Experimental Materials and Methods

Fine alumina powder ( $\text{Al}_2\text{O}_3$ - $\alpha$ , 100 nm, TM-DAR grade, TAIMEI, Tokyo, Japan) characterized by low sintering temperature (approximately 1250 °C), zirconia powder partially stabilized with yttrium oxide ( $\text{ZrO}_2 + 3\% \text{Y}_2\text{O}_3$ , 40 nm, TZ-3Y-E grade, Tosoh, Japan), and cBN powder (3–6  $\mu\text{m}$ , Micron+ABN grade, Element Six, Ireland) were used as the starting materials. The mixtures (vol.%) were prepared using a Fritsch Pulverisette 6 planetary ball mill equipped with a zirconia grinding vessel and balls. The milling process lasted for 2 h at 200 rpm. Acetone was used as the wetting medium. After drying, the mixtures were sieved and granulated using a 0.5 mm mesh.

Pure matrix ( $\text{Al}_2\text{O}_3 + 30\% \text{ZrO}_2$ ), as well as the composites, were treated via SPS, employing HPD5 type equipment (manufactured by FCT Systeme GmbH, Germany). The powders were placed in a graphite die (inner diameter of 20 mm), then uniaxially pressed at 63 MPa, and heated to the sintering temperature at a heating rate of 100 °C/min. A graphite sheet, 0.5 mm in thickness, was inserted between the raw material powder and graphite die to prevent scuffing of the punch and to ease the extraction of the sintered sample from the matrix. The graphite die was also wrapped in carbon blankets to

minimize heat loss during sintering. The samples were sintered in the temperature range 1150–1500 °C for 4 min in Ar.

Apparent densities of the sintered samples were determined by the Archimedes method in distilled water. Specimens for microstructure examination were prepared by routine ceramographic procedure, they were cut, ground, and polished to a 1 µm finish. The microstructural characterization was determined by scanning electron microscopy (FIB-SEM ZEISS AURIGA Compact). The areas of individual phases were processed by image analysis in software Fiji, and grain diameters were determined from the average grain area with the assumption that the grains are circular.

Mechanical characterization was performed in terms of measurement of basic mechanical properties of bulk materials such as hardness and crack-extension resistance using indentation methods. Hardness was determined by Vickers indentation (Wolpert Wilson 432 SVD Vickers Hardness Tester) under a load of 9.81 N with a dwell time of 15 s. In order to determine the crack-extension resistance, at least 10 Vickers imprints per specimen were introduced with the load 98.07 N. The crack-extension resistance was calculated from the lengths of radial cracks and indents diagonals using a formula (Equation (1)) valid for semi-circular crack systems as proposed by Anstis et al. [22].

$$K_{I,IFR} = 0.016 \cdot \left(\frac{E}{H}\right)^{1/2} \cdot \left(\frac{P}{c^{3/2}}\right) \quad (1)$$

where  $K_{I,IFR}$ —indentation toughness ( $\text{MPa}\cdot\text{m}^{1/2}$ ), 0.016—material-independent constant for Vickers-produced radial cracks,  $E$ —Young's modulus (GPa),  $H$ —Vickers hardness (GPa),  $P$ —indentation load (N),  $c$ —half-length of the radial crack (m).

Nanoindentation was carried out on polished surfaces of the composites using a Berkovich diamond tip on an Agilent G200 NanoIndenter. Continuous stiffness measuring (CSM) mode was applied with a maximum depth of 200 nm and a strain rate of  $0.05 \text{ s}^{-1}$ . On each system, 100 indents were prepared, arranged in  $10 \times 10$  arrays with a distance between the indents of 6 µm. The hardness and modulus were automatically calculated according to the standards of instrumented indentation (Oliver–Pharr method), [23]. The tip was calibrated prior to the measurement on fused silica, which resulted in an accurate tip area function over  $\sim 30 \text{ nm}$ .

### 3. Results and Discussion

The optimization of sintering temperature was made for each composition. Similarly, as in the report [21], the values of density and Young's modulus formed the preliminary criteria for the assessment of the consolidation degrees of the sintered compacts. We found interesting differences in SPS sintering behavior of pure  $\text{Al}_2\text{O}_3$ – $\text{ZrO}_2$  oxide-matrix in comparison to the sintering behavior of the  $\text{Al}_2\text{O}_3$ – $\text{ZrO}_2$ –cBN composites, Figure 1. According to the results illustrated in Figure 1, the addition of cBN to  $\text{Al}_2\text{O}_3$ – $\text{ZrO}_2$  matrix resulted in a decrease in sintering temperature. What is interesting is that this phenomenon has not been observed for composites having only one oxide in the matrix ( $\text{Al}_2\text{O}_3$ –cBN or  $\text{ZrO}_2$ –cBN), [21].

As is visible in Figure 1, both the density (Figure 1a) and Young's modulus curves (Figure 1b) show a maximum for the  $\text{Al}_2\text{O}_3$ – $\text{ZrO}_2$  matrix at the temperature of approximately 1400 °C, while a similar maximum was found for the  $\text{Al}_2\text{O}_3$ – $\text{ZrO}_2$ –cBN composites at the temperature approximately 1200 °C. In the case of the  $\text{Al}_2\text{O}_3$ – $\text{ZrO}_2$  matrix, with increasing temperature, the density and Young's modulus is approximately constant, on the other side, in the case of composites with cBN, both the density and Young's modulus are decreasing with the increasing temperature. This decrease is more significant in the case of Young's modulus. Based on the results illustrated in Figure 1, with the aim to use the lowest sintering temperature possible to avoid the cBN–hBN phase transformation but guaranteeing high density and elastic modulus, the sintering temperature for the  $\text{Al}_2\text{O}_3$ – $\text{ZrO}_2$  and  $\text{Al}_2\text{O}_3$ – $\text{ZrO}_2$ –cBN systems were selected as 1400 °C and 1250 °C, respectively.

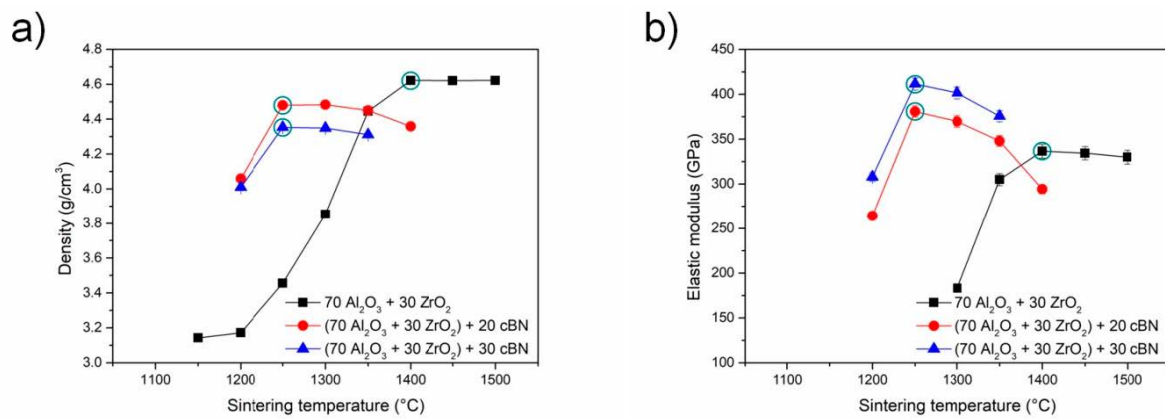


**Figure 1.** Density (a) and Young's modulus (b) of composites sintered via SPS with different temperatures measured at room temperature after the sintering. The experimental data in circles illustrate the sintering temperatures for the systems used for investigation in the present study.

The results of the microstructure analyses of the investigated systems are illustrated in Figures 2–4 and Table 1. In Figure 2, we show characteristic microstructures of the Al<sub>2</sub>O<sub>3</sub>–ZrO<sub>2</sub> system at different magnifications and the results of the statistical analyses of the individual grain size/area. It is evident that the system is very homogenous without the presence of larger defects in the form of pores, voids, clusters of grains, or large grains. The area of Al<sub>2</sub>O<sub>3</sub> grains changes from 0.01 to 0.07 μm<sup>2</sup> with an average grain area of 0.035 μm<sup>2</sup>, considering that circular grains are approximately 0.22 μm in diameter. The ZrO<sub>2</sub> grains are smaller, with a diameter of approximately 0.15 μm.

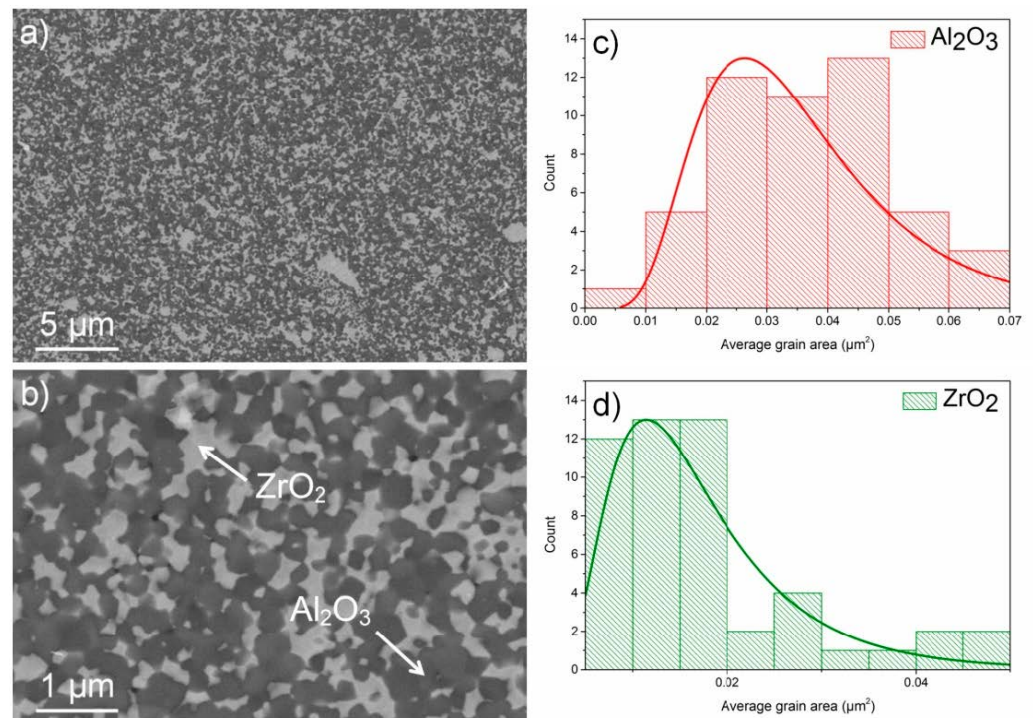


**Figure 2.** Microstructure (a,b) and grain size distribution (c,d) of Al<sub>2</sub>O<sub>3</sub> + ZrO<sub>2</sub> system.

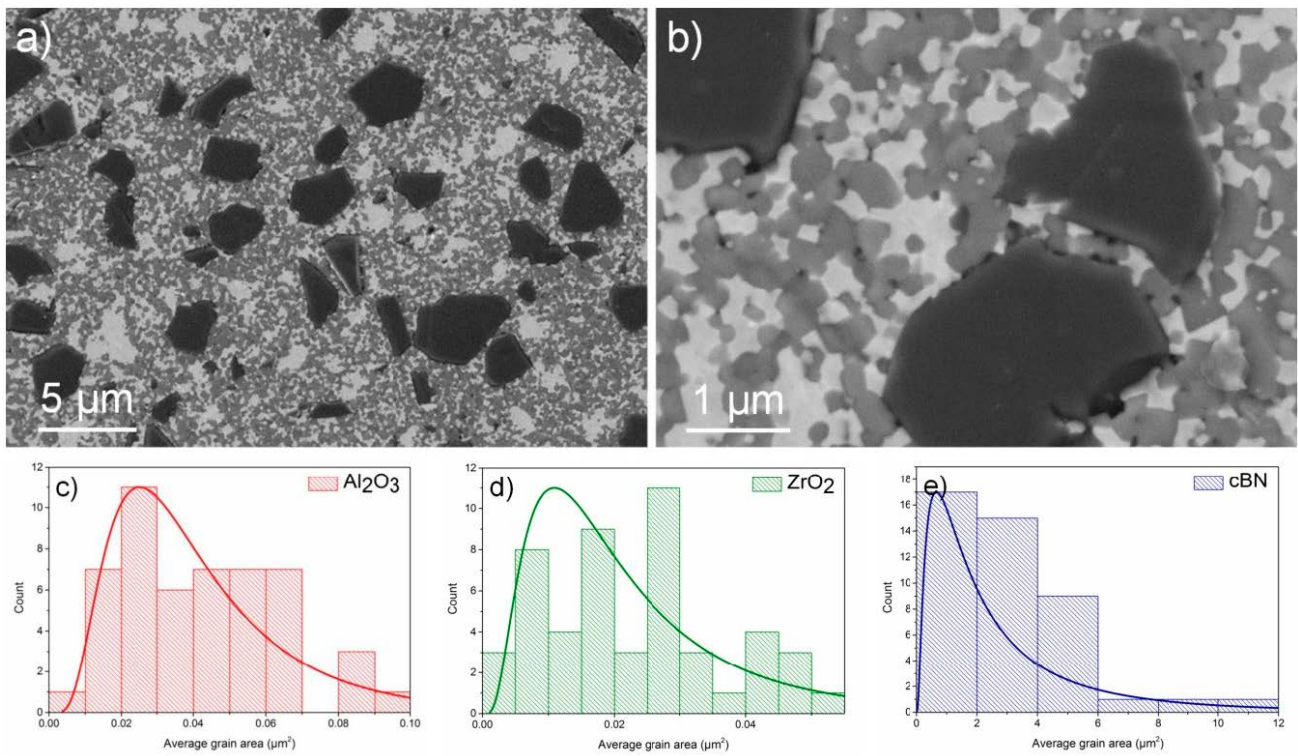


Figure 3. Microstructure (a,b) and grain size distribution (c–e) of  $\text{Al}_2\text{O}_3 + \text{ZrO}_2 + 20\% \text{cBN}$  system.

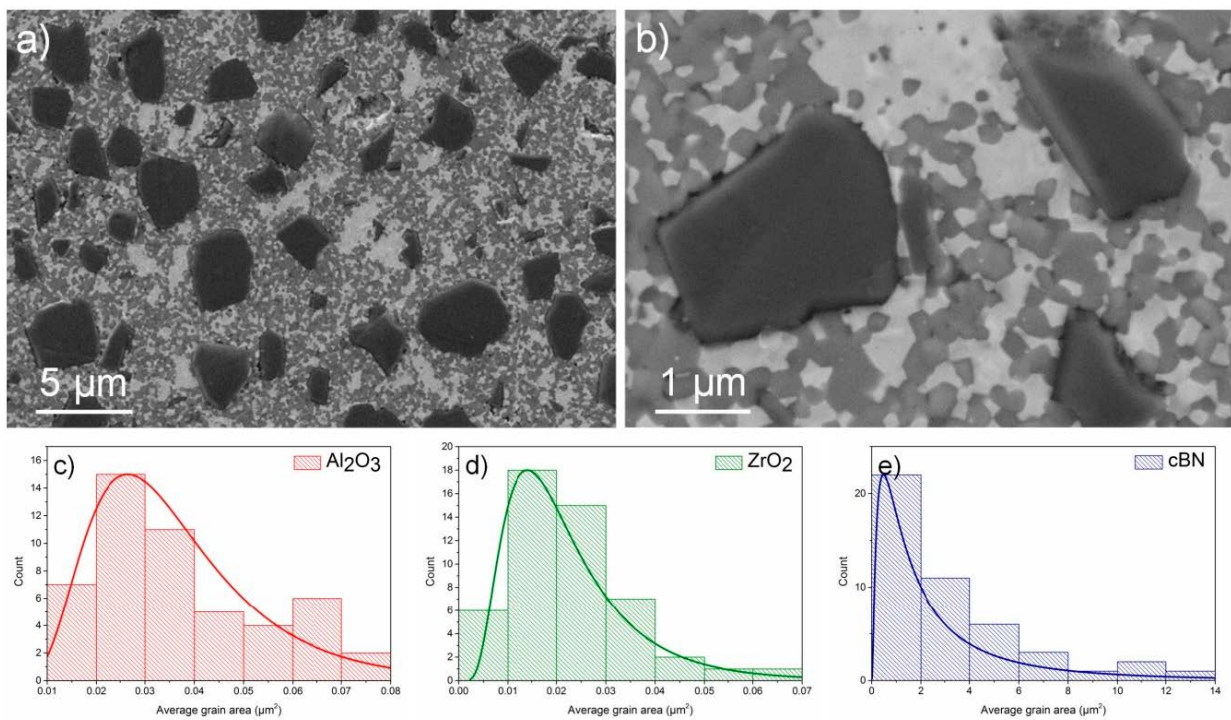


Figure 4. Microstructure (a,b) and grain size distribution (c–e) of  $\text{Al}_2\text{O}_3 + \text{ZrO}_2 + 30\% \text{cBN}$  system.

**Table 1.** Parameters of the investigated materials.

Composition (Vol.%)	Sintering Temperature, T (°C)	Density (g/cm <sup>3</sup> )	Young's Modulus (GPa)	Al <sub>2</sub> O <sub>3</sub> Grain Diameter (µm)	ZrO <sub>2</sub> Grain Diameter (µm)	cBN Grain Diameter (µm)
70 Al <sub>2</sub> O <sub>3</sub> + 30 ZrO <sub>2</sub>	1400	4.62 ± 0.01	337 ± 8	0.21	0.15	–
(70 Al <sub>2</sub> O <sub>3</sub> + 30 ZrO <sub>2</sub> ) + 20 cBN	1250	4.48 ± 0.006	381 ± 7	0.23	0.17	1.90
(70 Al <sub>2</sub> O <sub>3</sub> + 30 ZrO <sub>2</sub> ) + 30 cBN	1250	4.35 ± 0.006	412 ± 7	0.22	0.17	1.84

Characteristic microstructure and grain size distribution of the Al<sub>2</sub>O<sub>3</sub>–ZrO<sub>2</sub> system with 20 vol% cBN addition is illustrated in Figure 3. The microstructure of the Al<sub>2</sub>O<sub>3</sub>–ZrO<sub>2</sub> matrix is similar to the microstructure of the system without cBN addition, only seems to be more heterogenous mainly as regarding the ZrO<sub>2</sub> phase with grain size changing from 100 nm to 1.0 µm. These relatively large ZrO<sub>2</sub> grains probably appeared as a result of the regrinding of the grinding vessel made of ZrO<sub>2</sub> by super abrasive cBN particles.

The size of the cBN grains, well distributed in the Al<sub>2</sub>O<sub>3</sub>–ZrO<sub>2</sub> matrix, changing from approximately 0.4 to 3 µm.

Similar is the microstructure of the Al<sub>2</sub>O<sub>3</sub>–ZrO<sub>2</sub> with 30 vol% cBN addition where the matrix shows the highest heterogeneity, mainly as regarding the ZrO<sub>2</sub> phase with grain size changing from 0.1 to 1.5 µm. The distribution in cBN grains in composites with cBN addition is similar and homogenous without clusters of cBN grains with a similar grain size of the cBN grains. Microstructure study of both Al<sub>2</sub>O<sub>3</sub>–ZrO<sub>2</sub>–cBN composites at higher magnification revealed weak contact between the cBN grains and the matrix. In many cases, but mainly at larger cBN grains, clear micro-cracks are visible at the grain/matrix interphase. Such weak interphase (as we see later) positively influences the crack deflection, but this mechanism is not effective enough in the toughening process.

The influence of the cBN addition on the hardness of the composites is illustrated in Table 2. As is visible, the hardness is slightly increasing with the addition of 20% and 30% cBN additives from 16.18 to 16.86 GPa and 17.10 GPa, respectively. The hardness improvement, similarly as was reported by other authors for similar systems, is not so remarkable.

**Table 2.** Properties of the investigated materials.

Composition (Vol.%)	Hardness HV1 (GPa)	K <sub>I,IFR</sub> (MPa.m <sup>1/2</sup> )	Nanohardness of Matrix (GPa)	Nanohardness of cBN (GPa)	Indentation Modulus of Matrix (GPa)	Indentation Modulus of cBN (GPa)
70 Al <sub>2</sub> O <sub>3</sub> + 30 ZrO <sub>2</sub>	16.18 ± 0.44	3.72 ± 0.41	29.5 ± 3	–	410 ± 20	–
(70 Al <sub>2</sub> O <sub>3</sub> + 30 ZrO <sub>2</sub> ) + 20 cBN	16.86 ± 0.57	4.03 ± 0.20	30.6 ± 4	68.5 ± 7	420 ± 25	775 ± 40
(70 Al <sub>2</sub> O <sub>3</sub> + 30 ZrO <sub>2</sub> ) + 30 cBN	17.10 ± 0.77	4.29 ± 0.53	30.8 ± 4	70.2 ± 8	430 ± 25	780 ± 50

The influence of the cBN addition on the crack-extension resistance of the investigated materials, measured using the IF method, is visible in Table 2. The results revealed increased indentation toughness with increased cBNs addition from 3.72 to 4.29 MPa.m<sup>1/2</sup>. Micro-fractography of the fracture lines revealed the reason for the fracture toughness improvement in the investigated systems, Figure 5. The results show that in the Al<sub>2</sub>O<sub>3</sub> + ZrO<sub>2</sub> matrix, the crack propagation is 100% intergranular, due to the nanometric grain size of both the Al<sub>2</sub>O<sub>3</sub> and ZrO<sub>2</sub> grains with no sign of toughening mechanisms in the form of crack deflection or crack bridging, characteristic, e.g., for silicon nitride ceramics with elongated beta-Si<sub>3</sub>N<sub>4</sub> grains.

The presence of cBN grains in the composites initiated different toughening mechanisms (Figure 5), mainly crack deflection, very similar for both investigated systems, only the frequency of their occurrence is slightly different. However, in both investigated composites, the crack deflection is not so effective, which probably is connected with the mentioned weak cBN/matrix interphase. This weak interphase results in an easily created crack deflection, which energetically contributes less to the toughness improvement.

As it is visible, the crack direction changes due to the interaction with the cBN grains and parallel with the main crack often second cracks are visible, arising due to the transgranular failure of the cBN grains. This is observed not only in the case of large grains with a size of different micrometers but also in the case of small cBN grains with a size around or lower than one micrometer. This crack branching is, however, also not so effective from the point of view of toughening, because of the very brittle cBN grains and low energy transgranular fracture.

The observed toughening mechanisms are in full agreement with the published results on ceramic + cBN systems. Crack deflections caused by the hard cBN particles were observed in many composites processed by SPS [18,19]. The fracture toughness of SiO<sub>2</sub>, Al<sub>2</sub>O<sub>3</sub>, and TiN was increased by incorporating 20 vol% cBN into their microstructure, mainly the fracture toughness of SiO<sub>2</sub> 20 vol% cBN composite where the increase was from 0.6 to 1.5 MPa.m<sup>1/2</sup>. In the case of Al<sub>2</sub>O<sub>3</sub> + cBN system, improvement was also significant from 2.7 to 4.1 MPa.m<sup>1/2</sup>, sintered at 1300 °C for 600 s. In this system, crack deflection was also observed around the cBN grains, which possibly has resulted in the increase in fracture toughness. On the other hand, it was observed that cracks propagated straight through BN grains and resulted in the transformation of grains from cBN to hBN.

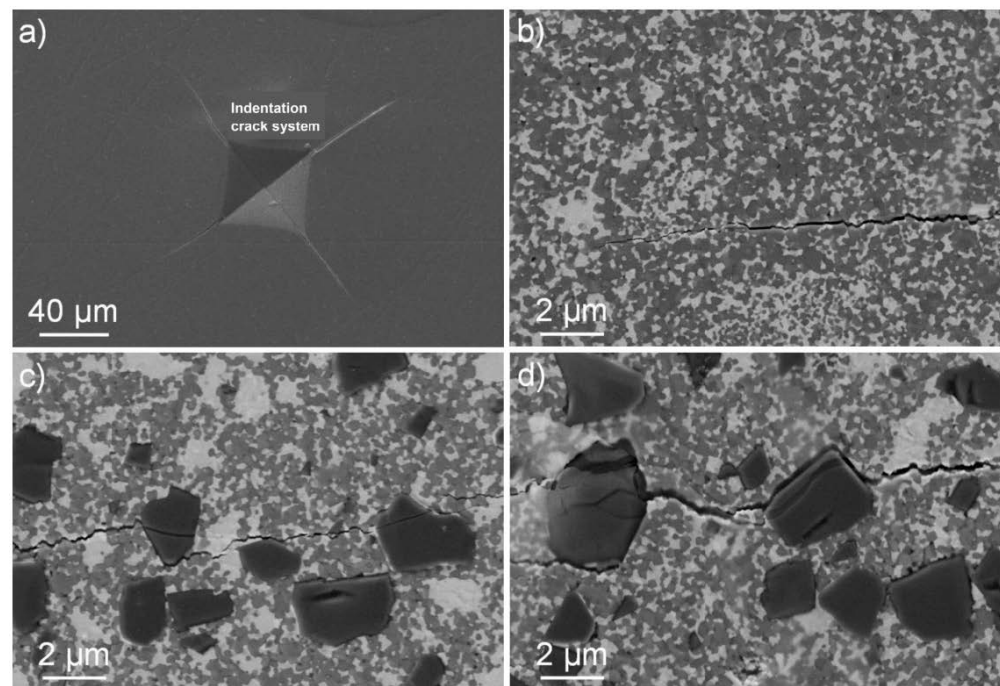


**Figure 5.** Indentation crack system (a) and characteristic fracture mechanisms in Al<sub>2</sub>O<sub>3</sub> + ZrO<sub>2</sub> (b) and Al<sub>2</sub>O<sub>3</sub> + ZrO<sub>2</sub> + 20% cBN system (c,d).

Characteristic hardness–displacement and indentation modulus–displacement relationships arising during the nanoindentation of Al<sub>2</sub>O<sub>3</sub> + ZrO<sub>2</sub> and Al<sub>2</sub>O<sub>3</sub> + ZrO<sub>2</sub> + 30% cBN systems are illustrated in Figure 6. The curves are selected as curves connected with the indentation of matrix or cBN grains based on SEM observation of the indented surface without information on which phases are in close vicinity below the indent.

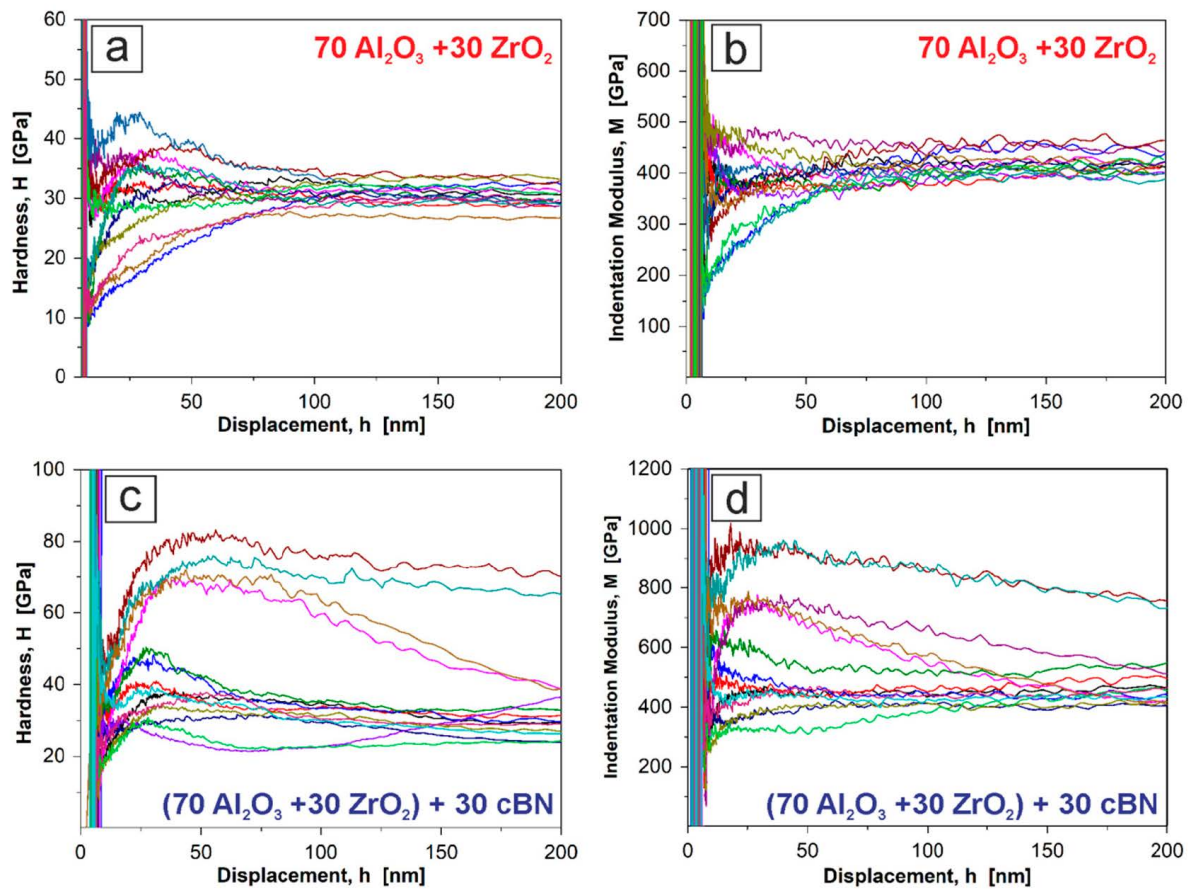


**Figure 6.** Hardness–displacement and indentation modulus–displacement relationships during nanoindentation of  $\text{Al}_2\text{O}_3 + \text{ZrO}_2$  (a,b) with red label and  $\text{Al}_2\text{O}_3 + \text{ZrO}_2 + 30\% \text{ cBN}$  systems, (c,d) with blue label.

In the case of  $\text{Al}_2\text{O}_3 + \text{ZrO}_2$  matrix, the hardness–displacement curves up to 100 nm depth show significant scatter, but the curves from 100 to 200 nm are very similar and the nanohardness at 200 nm is very reproducible with the value of  $29.5 \pm 3 \text{ GPa}$ . The indentation modulus–displacement curves are very similar and at 200 nm give the result of  $410 \pm 20 \text{ GPa}$  for the matrix system.

A slightly different situation is visible in the case of  $\text{Al}_2\text{O}_3 + \text{ZrO}_2 + \text{cBN}$  composites during the measuring of the hardness of  $\text{Al}_2\text{O}_3 + \text{ZrO}_2$  matrix where the behavior is influenced by the present cBN particles around, below the indents, at different distances, which is visible in the case of hardness–displacement but more significantly in the case of indentation modulus curves. This results show that the average nanohardness values for the  $\text{Al}_2\text{O}_3 + \text{ZrO}_2$  matrix are a little higher in comparison to the  $\text{Al}_2\text{O}_3 + \text{ZrO}_2$  system with a value of  $30.6 \pm 4 \text{ GPa}$  and  $30.8 \pm 4 \text{ GPa}$  for the systems with 20 wt% and 30 wt% cBN, respectively. A similar higher scatter is in the indentation modulus–displacement curves and resulted in an approximate indentation modulus value  $425 \pm 25 \text{ GPa}$ .

Characteristic nanoindentation with the corresponding load–displacement, hardness–displacement and indentation modulus–displacement curves for the  $\text{Al}_2\text{O}_3 + \text{ZrO}_2$  system is illustrated in Figure 7. No visible pop-in effect was found during the indentation, however, the hardness–displacement and indentation modulus–displacement curves show some slight irregularities.

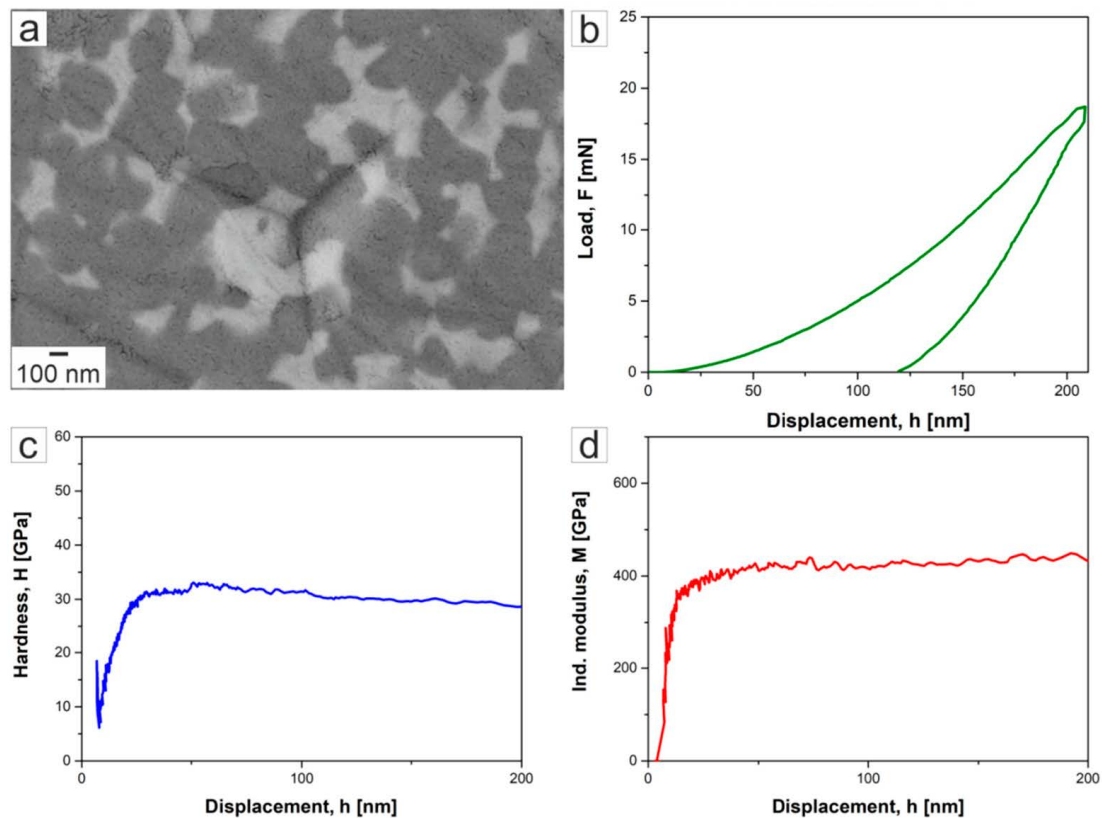


**Figure 7.** Characteristic nanoindentation of  $\text{Al}_2\text{O}_3 + \text{ZrO}_2$  matrix with an imprint (a), load–displacement (b), hardness–displacement (c), and indentation modulus–displacement (d) curves.

Among the first, Krell and Schadlich [24] investigated the nanoindentation characteristics of a submicrometer grained alumina ceramics with different residual porosity at loads of 20–200 mN. According to the results, at small testing loads of 25–50 mN, the Vickers hardness of the ceramics with low porosity were changing from 25 to 30 GPa, depending on the microstructure of the systems.

Mao et al. [25] investigated the nanoscale pop-in phenomena in polycrystalline alumina and alumina single crystal using nanoindentation with Berkovich indenter. They found strong ISE in hardness values within the indentation range from 0.0 to 100 nm, i.e., the measured hardness values decreased with increasing indentation depth. In the ISE region, the average hardness was  $46.7 \pm 15$  GPa for  $\text{Al}_2\text{O}_3$  single crystal and  $41.7 \pm 5.0$  GPa for polycrystalline alumina. In the load-independent hardness region, they found  $27.5 \pm 2$  GPa hardness for  $\text{Al}_2\text{O}_3$  single crystal and  $30 \pm 3$  GPa for polycrystalline alumina.

Recently, Aragón-Duarte et al. [26] studied the nanomechanical properties of several oxide ceramics—80 wt%  $\text{Al}_2\text{O}_3 + 20$  wt% TZ-3Y, (ZTA), 20 wt%  $\text{Al}_2\text{O}_3 + 80$  wt% TZ-3Y, (ATZ) tetragonal polycrystalline zirconia (3Y-TZP), and cubic stabilized zirconia (8Y-CSZ), using nanoindentation before and after low temperature ageing/degradation. A Berkovich diamond indenter with a tip radius of  $20 \pm 5$  nm was used at low loads of 1.5, 2, and 5 mN and strain rate of  $0.05 \text{ s}^{-1}$ . The ZTA (80 wt%  $\text{Al}_2\text{O}_3 + 20$  wt% TZ-3Y) with an average grain size of 495 nm, which is very similar to the  $\text{Al}_2\text{O}_3 + \text{ZrO}_2$  system in the present investigation, shows elastic modulus of  $360 \pm 6$  GPa and nanohardness of  $35 \pm 1$  GPa. These values are very close to the values of hardness and elastic modulus measured for the investigated system in our experiment.

Very interesting is the hardness vs. indentation depth and indentation modulus vs. indentation depth curves during the nanoindentation of cBN grains in the cBN containing composites with significantly higher scatter in comparison to the behavior of the  $\text{Al}_2\text{O}_3 + \text{ZrO}_2$  matrix (Figure 6c,d). As it is illustrated, the hardness of the cBN grains

shows maximum at approximately 50 nm indentation depth with values from 65 to 85 GPa. With increasing the indentation depth, the hardness is decreasing, with different hardness values showing at 100 nm depth in the range from 55 to 77 GPa and at 200 nm from 40 to 75 GPa. Even higher scatter was found in the indentation modulus with highest values at approximately 25–30 nm depth with values from 710 to 950 GPa, which decreases with increasing indentation depth and at 100 nm show values from 550 to 700 GPa and at 200 nm depth values from approximately 400 to 800 GPa.

Characteristic nanoindentation with the corresponding load–displacement, hardness–displacement, and indentation modulus–displacement curves for the  $\text{Al}_2\text{O}_3 + \text{ZrO}_2 + 30\%$  cBN system is illustrated in Figure 8. The indent was selected very carefully to show representant nanohardness characteristics for the cBN grain. No visible pop-in effect was found during the indentation and the curves show characteristic load–size effect.

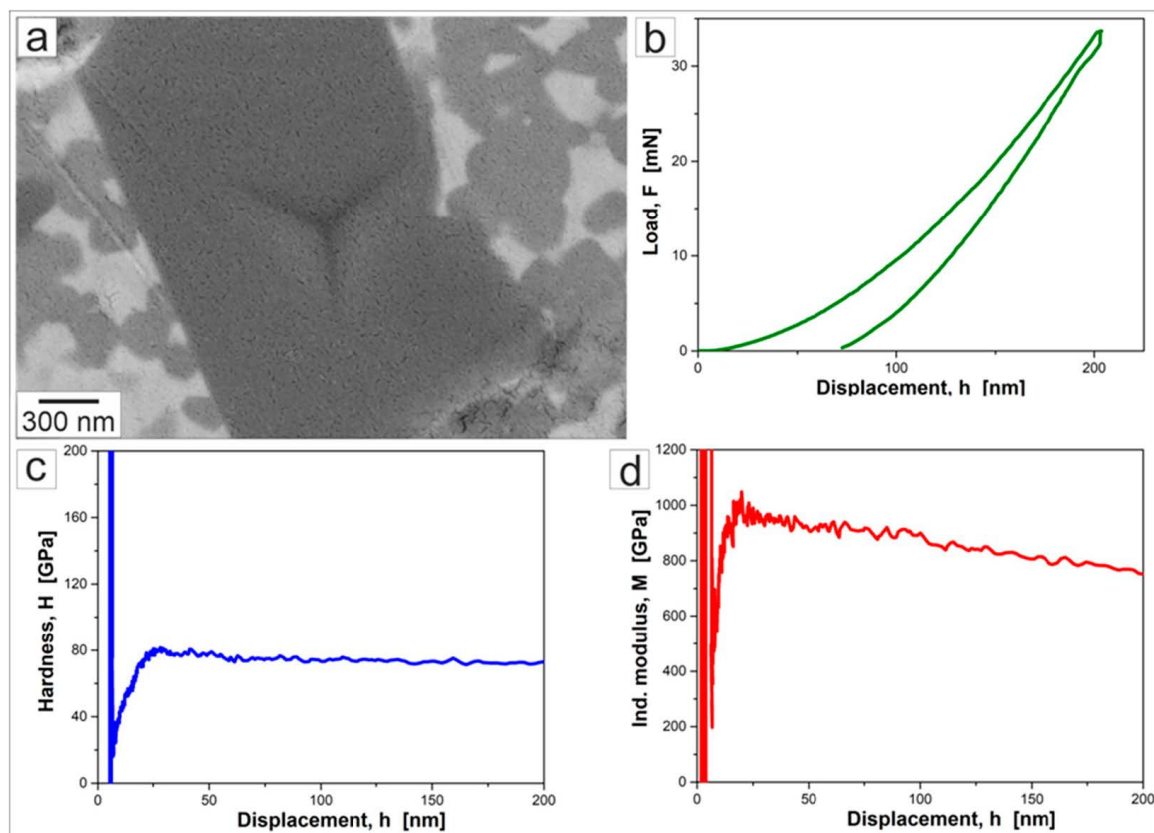


**Figure 8.** Characteristic nanoindentation of cBN grain in  $\text{Al}_2\text{O}_3 + \text{ZrO}_2 + 30\%$  cBN composite, imprint (a), load–displacement (b), hardness–displacement (c), and indentation–displacement (d) curves.

Recently, Dub et al. [27] investigated the characteristics of the elastoplastic transition in the contact region during the nanoindentation of cBN systems with different degrees of crystal structure perfection. For the investigation, they used the (111) face of a cBN single crystal with the ideal structure and polycrystalline nanograined cBN in which the separate grains are characterized by the existence of nanotwinned interlayers. The nanoindentation was performed using Berkovich indenter with the tip radius  $R \approx 230$  nm in CSM mode with 200 nm indentation depth regime.

During the indentation of (111) cBN, single-crystal sharp increase of the contact depth by approximately 10 nm (pop-in) was observed at the indentation depth of  $\sim 75$  nm. This indicates that at the load of 35 mN, a plastic deformation occurred in the contact. The critical load of the pop-in formation changes from 5.5 to 10.3 mN with an average value of  $8.3 \pm 1.5$  mN. If the tests are performed at loads lower than the critical load, the loading cycle is fully reversible, therefore, a pop-in at the starting region of the loading corresponds

to the transition from the elastic to elastoplastic deformation in the contact, and the indenter penetration curve before a pop-in is a region of the elastic deformation in the contact.

During the nanoindentation of polycrystalline nanograined cBN surface, the depth of the indenter penetration gradually increased with the load without the pop-in appearance in the loading curve, probably as the result of the high density of the sample structure imperfection. The measured average mechanical properties—elastic modulus, hardness and critical shear stress—for (111) cBN single crystal are 960, 62, and 39 GPa, respectively. These mechanical properties for polycrystalline nanograined cBN are 971, 71, and 24 GPa, respectively.

Deura et al. [28] recently prepared bulk crystal of wurtzite-type boron nitride by the direct conversion method and performed nanoindentation measurements on the c-plane of the w-BN crystal at room temperature with the aim to evaluate the hardness and Young's modulus. They reported values for hardness and indentation modulus  $54 \pm 2$  and  $860 \pm 40$  GPa, respectively.

Very recently, Besharatloo et al. [29] performed a systematic investigation on micromechanical properties of the constitutive phases of a commercial polycrystalline cubic boron nitride-based BN-TiN ceramic/ceramic composite. Through the nanohardness testing and statistical evolution of the hardness results, they revealed three distinct groups of hardness values corresponding to the TiN matrix phase, cBN particles and a group with „mix-mode“ boundary phase under the indents. The reported average nanohardness values for the TiN binder, cBN grains, and boundary phase were 20, 50, and 35 GPa, respectively. In a combination of the nanomechanical testing results and results of advanced characterization techniques (EPMA and FESEM), they found different intrinsic hardness values for cBN particles as a function of phase (B/N ratio) stoichiometry. For BN grains with low N content, for stoichiometric grains and grains with high N content, they reported average hardness values of 43, 49, and 54 GPa, respectively.

Our results, as regards the hardness and indentation modulus of the cBN grains, are in agreement with the results of these reports. There are different possible reasons for such a high scatter in our results concerning the nanohardness and indentation modulus of cBN grains: The presence of the matrix phase with significantly different hardness and elastic modulus in the deformed volume (or in the very close distance) below the indentation, the existence of orientation dependence during the nanohardness measurement of cBN grains, different chemical composition of BN grains, or cBN to hBN phase transformation during the indentation of boron nitride grains. Evidently, the main reason is the “heterogeneity of the system”, which in the case when the microstructure parameters, as the grain size of the cBN grains, are very close to the size of the indent results in high scatter of hardness and indentation modulus. The other reasons, as the possible influence of phase transformation during the indentation, orientation dependent hardness of cBN, phase (B/N ratio) stoichiometry, etc., will be the subject of our future investigation.

#### 4. Conclusions

The aim of the present contribution was the processing of  $\text{Al}_2\text{O}_3 + \text{ZrO}_2 + \text{cBN}$  composites with an optimized processing route and to investigate the influence of cBN addition on their microstructure characteristics, microhardness, and crack-extension resistance. The other aim was to study the nanohardness of the  $\text{Al}_2\text{O}_3 + \text{ZrO}_2$  matrix and cBN grains.

1.  $\text{Al}_2\text{O}_3 + 30$  vol%  $\text{ZrO}_2$  matrix composites with 20 and 30 vol% cBN have been prepared with an optimized processing route, using spark plasma sintering (SPS) at temperatures of 1400 °C and 1250 °C.
2. The  $\text{Al}_2\text{O}_3 + \text{ZrO}_2$  matrix consists of alumina and zirconia grains with a grain diameter of approximately 220 and 160 nm with approximately 1.9  $\mu\text{m}$  cBN grains in the  $\text{Al}_2\text{O}_3 + \text{ZrO}_2 + \text{cBN}$  composites.
3. The microhardness of the  $\text{Al}_2\text{O}_3 + \text{ZrO}_2 + \text{cBN}$  composites are slightly increasing with cBN addition from 16.2 to 17.1 GPa and the crack-extension resistance from 3.72 to 4.29  $\text{MPa}\cdot\text{m}^{0.5}$  due to the toughening mechanisms in the form of crack deflection, crack branching and crack bridging.

4. The nanohardness and indentation modulus of the matrix are approximately 30 and 420 GPa and the cBN grains 70 and 777 GPa, respectively.

**Author Contributions:** Writing—original draft preparation: R.S.; writing—review and editing: J.D.; supervision: J.D.; investigation: R.S., M.I., P.K., P.W., M.P. and M.V. All authors have read and agreed to the published version of the manuscript.

**Funding:** This research was funded by the project M-ERA.NET 2 DURACER (Reference Number: project5014) and also the part of work was financed by the projects: APVV-19-0497, VEGA 2/0118/20, VEGA 1/0096/18, and “Research Centre of Advanced Materials and Technologies for Recent and Future Applications PROMATECH”, ITMS 26220220186, supported by the Operational Program “Research and Development” financed through European Regional Development Fund.

**Data Availability Statement:** Data is contained within the article.

**Acknowledgments:** R. S. acknowledges the support from the postdoctoral fellowship program: Supportive Fund of Štefan Schwarz for Creation of Postdoctoral Positions at Slovak Academy of Sciences.

**Conflicts of Interest:** The authors declare no conflict of interest.

## References

1. Dörre, E.; Hübner, H. *Alumina: Processing, Properties, and Applications*; Springer-Verlag: Berlin, Germany, 1984.
2. Morrell, R. *Handbook of Properties of Technical & Engineering Ceramics. Part 2. Data Reviews, Section 1. High-Alumina Ceramics*; The Stationery Office Books: London, UK, 1987.
3. Krell, A.; Blank, P.; Ma, H.; Hutzler, T.; van Bruggen, M.P.B.; Apetz, R. Transparent sintered corundum with high hardness and strength. *J. Am. Ceram. Soc.* **2003**, *86*, 12–18. [[CrossRef](#)]
4. Yoshimura, M.; Bowen, H.K. Electrical Breakdown Strength of Alumina at High Temperatures. *J. Am. Ceram. Soc.* **1981**, *64*, 404–410. [[CrossRef](#)]
5. Evans, A.G.; Cannon, R.M. Toughening of brittle solids by martensitic transformations. *Acta Metall.* **1986**, *34*, 761–800. [[CrossRef](#)]
6. Claussen, N. Fracture Toughness of Al<sub>2</sub>O<sub>3</sub> with an Unstabilized ZrO<sub>2</sub> Dispersed Phase. *J. Am. Ceram. Soc.* **1976**, *59*, 49–51. [[CrossRef](#)]
7. de Aza, A.H.; Chevalier, J.; Fantozzi, G.; Schehl, M. Torrecillas, Slow-crack-growth behavior of zirconia-toughened alumina ceramics processed by different methods. *J. Am. Ceram. Soc.* **2003**, *86*, 115–120. [[CrossRef](#)]
8. Fan, K.; Pastor, J.Y.; Ruiz-Hervias, J.; Gorauski, J.; Baudin, C. Determination of mechanical properties of Al<sub>2</sub>O<sub>3</sub>/Y-TZP ceramic composites: Influence of testing method and residual stresses. *Ceram. Int.* **2016**, *42*, 18700–18710. [[CrossRef](#)]
9. Wang, H.Z.; Gao, L.; Guo, J.K. Fabrication and microstructure of Al<sub>2</sub>O<sub>3</sub>-ZrO<sub>2</sub>(3Y)-SiC nanocomposites. *J. Eur. Ceram. Soc.* **1999**, *19*, 2125–2131. [[CrossRef](#)]
10. Chen, X.; Luo, L.; Liu, L.; Li, J.; Yu, H.; Li, W.; Chen, Y. Microstructure and mechanical properties of hot-pressed Al<sub>2</sub>O<sub>3</sub>-mullite-ZrO<sub>2</sub>-SiC composites. *Mater. Sci. Eng. A* **2019**, *740*, s390–s397. [[CrossRef](#)]
11. Zhang, J.; Tu, R.; Goto, T. Cubic boron nitride-containing ceramic matrix composites for cutting tools. *Adv. Ceram. Matrix Compos.* **2014**, 570–586. [[CrossRef](#)]
12. Klimczyk, P.; Figiel, P.; Petrusa, I.; Olszyna, A. Cubic boron nitride based composites for cutting applications. *J. Achiev. Mater. Manuf. Eng.* **2011**, *44*, 198–204.
13. Garrett, J.C.; Sigalas, I.; Wolfrum, A.K.; Herrmann, M. Effect of cubic boron nitride grain size in the reinforcing of  $\alpha$ -Sialon ceramics sintered via SPS. *J. Eur. Ceram. Soc.* **2015**, *35*, 451–462. [[CrossRef](#)]
14. Shonhiwa, A.; Herrmann, M.; Sigalas, I.; Coville, N. Reaction bonded aluminum oxide composites containing cubic boron nitride. *Ceram. Int.* **2009**, *35*, 909–911. [[CrossRef](#)]
15. Hotta, M.; Goto, T. Densification and microstructure of Al<sub>2</sub>O<sub>3</sub>-cBN composites prepared by spark plasma sintering. *J. Ceram. Soc. Japan* **2008**, *116*, 744–748. [[CrossRef](#)]
16. Petrusa, I.A. Features of a cBN-to-graphite-like BN phase transformation under pressure. *Diam. Relat. Mater.* **2000**, *9*, 1487–1493. [[CrossRef](#)]
17. Solozhenko, V.L.; Turkevich, V.Z.; Holzapfel, W.B. Refined Phase Diagram of Boron Nitride. *J. Phys. Chem. B* **1999**, *103*, 2903–2905. [[CrossRef](#)]
18. Hotta, M.; Goto, T. Effects of cubic BN addition and phase transformation on hardness of Al<sub>2</sub>O<sub>3</sub>-cubic BN composites. *Ceram. Int.* **2011**, *37*, 1453–1457. [[CrossRef](#)]
19. Yaman, B.; Mandal, H. Spark plasma sintering of Co-WC cubic boron nitride composites. *Mater. Lett.* **2009**, *63*, 1041–1043. [[CrossRef](#)]

20. Irshad, H.M.; Ahmed, B.A.; Ehsan, M.A.; Khan, T.I.; Laoui, T.; Yousaf, M.R.; Ibrahim, A.; Hakeem, A.S. Investigation of the structural and mechanical properties of micro-/nano-sized Al<sub>2</sub>O<sub>3</sub> and cBN composites prepared by spark plasma sintering. *Ceram. Int.* **2017**, *43*, 10645–10653. [[CrossRef](#)]
21. Klimczyk, P.; Wyżga, P.; Cyboron, J.; Laszkiewicz-Lukasik, J.; Podsiadlo, M.; Cygan, S.; Jaworska, L. Phase stability and mechanical properties of Al<sub>2</sub>O<sub>3</sub>-cBN composites prepared via spark plasma sintering. *Diam. Relat. Mater.* **2020**, *104*, 107762. [[CrossRef](#)]
22. Anstis, G.; Chantikul, P.; Lawn, B.; Marshall, D. A critical evaluation of indentation techniques for measuring fracture toughness: I Direct crack measurements. *J. Am. Ceram. Soc.* **1981**, *46*, 533–538. [[CrossRef](#)]
23. Oliver, W.C.; Pharr, G.M. Measurement of hardness and elastic modulus by instrumented indentation: Advances in understanding and refinements to methodology. *J. Mater. Res.* **2004**, *19*, 3–20. [[CrossRef](#)]
24. Krell, A.; Schädlich, S. Nanoindentation hardness of submicrometer alumina ceramics. *Mater. Sci. Eng. A* **2001**, *307*, 172–181. [[CrossRef](#)]
25. Mao, W.G.; Shen, Y.G.; Lu, C. Deformation behavior and mechanical properties of polycrystalline and single crystal alumina during nanoindentation. *Scr. Mater.* **2011**, *65*, 127–130. [[CrossRef](#)]
26. Aragón-Duarte, M.C.; Nevarez-Rascón, A.; Esparza-Ponce, H.E.; Nevarez-Rascón, M.M.; Talamantes, R.P.; Ornelas, C.; Mendez-Nonell, J.; González-Hernández, J.; Yacamán, M.J.; Hurtado-Macías, A. Nanomechanical properties of zirconia-yttria and alumina zirconia-yttria biomedical ceramics, subjected to low temperature aging. *Ceram. Int.* **2017**, *43*, 3931–3939. [[CrossRef](#)]
27. Dub, S.N.; Petrusha, I.A.; Bushlya, V.M.; Taniguchi, T.; Belous, V.A.; Tolmachova, G.N.; Andreev, A.V. Theoretical shear strength and the onset of plasticity in nanodeformation of cubic boron nitride. *J. Superhard Mater.* **2017**, *39*, 88–98. [[CrossRef](#)]
28. Deura, M.; Kutsukake, K.; Ohno, Y.; Yonenaga, I.; Taniguchi, T. Nanoindentation measurements of a highly oriented wurtzite-Type boron nitride bulk crystal. *Jpn. J. Appl. Phys.* **2017**, *56*, 030301. [[CrossRef](#)]
29. Besharatloo, H.; Gordon, S.; Rodriguez-Suarez, T.; Can, A.; Oliver, W.C.; Llanes, L.; Roa, J.J. Small-scale mechanical properties of constitutive phases within a polycrystalline cubic boron nitride composite. *J. Eur. Ceram. Soc.* **2019**, *39*, 5181–5189. [[CrossRef](#)]